JAMES | Journal of Advances in Modeling Earth Systems

RESEARCH ARTICLE
10.1029/2019MS001820

Convection On the Edge

J. M. Windmiller[1] and C. Hohenegger[1]

[1]Max Planck Institute for Meteorology, Hamburg, Germany

Abstract Deep convection over tropical oceans often appears intensified at the edge of convectively active regions, both in idealized studies and in observations. This edge intensification of convection is studied in detail here, using the steady state of a radiative-convective equilibrium study, marked by a single convective cluster with deep convection intensified at the edge of this cluster. The cause for edge intensification and its dependence on the cluster area is investigated by comparing the spatial distribution of deep convection to different variables known to be important for convection. Analysis of the simulation suggests that the edge is marked by an increased probability for the triggering of convection rather than by stronger updrafts. In particular, while the edge of the moist region is not thermodynamically more favorable, we find strong surface convergence and therefore dynamical lifting at this edge. The surface convergence is shown to result from two opposing flows. On the one hand, there is, as expected from previous radiative-convective equilibrium simulations, a low-level inflow directed toward the moist region. On the other hand, there is a positive density anomaly at the surface which is the result of continuously forming cold pools within the convectively active region, creating a super-cold-pool. As the velocity of the low-level inflow approximately matches the potential propagation speed of the super-cold-pool boundary, these opposing flows explain the presence of strong convergence at the edge of this region. Whether the resulting lifting induces the formation of deep convection is shown to depend on the large-scale instability.

Key Points:
- Precipitation tends to intensify at the edge of the convectively active region if the region is large enough
- Edge intensification in a RCE simulation with a single convective cluster cannot be explained by spatial variations of CAPE or moisture
- Edge intensification in this case is linked to the formation of a super-cold-pool in the convective cluster balanced by a low-level inflow

Correspondence to:
J. M. Windmiller,
Julia.Windmiller@mpimet.mpg.de

Citation:
Windmiller, J. M., & Hohenegger, C. (2019). Convection on the edge. *Journal of Advances in Modeling Earth Systems*, *11*, 3959–3972. https://doi.org/10.1029/2019MS001820

Received 19 JUL 2019
Accepted 2 OCT 2019
Accepted article online 20 OCT 2019
Published online 8 DEC 2019

1. Introduction

In the tropical atmosphere, there is a tight relationship between the distribution of water vapor and the location of deep convection. Over tropical oceans, in particular, there is a strong correlation between deep convection (as measured by precipitation rate) and the column-integrated water vapor content (CWV; e.g., Bretherton et al., 2004). The humidity field and the spatial distribution of convection have, moreover, been found to evolve in parallel in idealized simulations of the tropical atmosphere in which, in the absence of any lateral energy transport, radiative cooling is balanced by convective heating. In particular, many of these so-called radiative-convective equilibrium (RCE) studies show self-aggregation of convection (e.g., Bretherton et al., 2005), which is described by the formation and upscale growth of moist and dry regions with deep convection limited to the moist regions. The steady state of these studies is, in fact, often described by a single moist region in which all the deep convection occurs and which is surrounded by a dry region without deep convection. Due to this close relationship between convection and the humidity field, self-aggregation of convection is often analyzed in terms of the fields describing the spatial distribution of humidity rather than convection (e.g., Wing & Cronin, 2016).

Yet, considering the RCE study of Hohenegger and Stevens (2016), the spatial distribution of deep convection within the region of deep convective activity is not random but becomes increasingly intensified at the edge of this region during the later stages of self-aggregation (see their Figure 1 from about Day 20 onward). Signs of more intense deep convection at the edge of the final self-aggregation cluster can also be found in other RCE studies, see Figure 1 in Becker et al. (2018), Figure 4.2 in Müller (2019), Figure 8 in Wing et al. (2018), and Figure 2c in Patrizio and Randall (2019). This edge intensification of deep convection is also present in other convection-permitting simulations using less idealized setups. Liu and Moncrieff M. W. (2008), for example, performed a two-dimensional RCE-like simulation but with a lower boundary, which has a positive sea surface temperature (SST) anomaly in the center of the domain. While deep convection is limited to the region of high SST, as expected from previous studies (e.g., Tompkins, 2001a), the peak precipitation rate is found near the edge of the region, which contains precipitation rather than in the interior of this region. Another instance of edge intensification can be found in an aqua-patch simulation performed by Nolan et al. (2016). Performing a convection-permitting simulation with a zonally symmetric SST profile close to

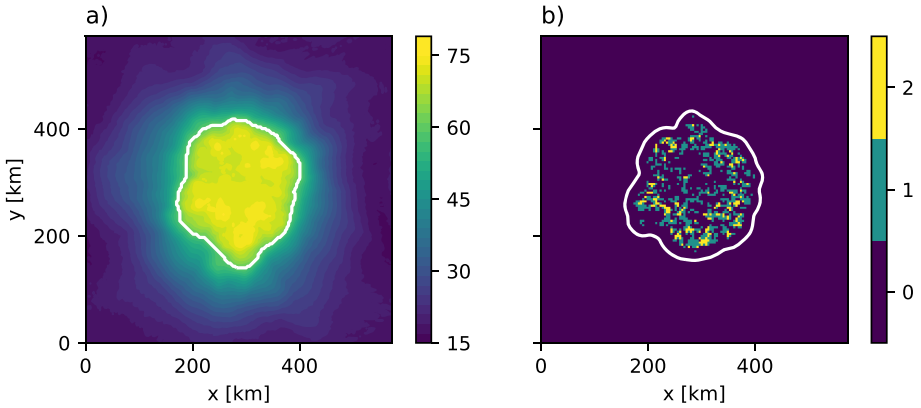

Figure 1. Snapshots of (a) the daily averaged water vapor content field (mm) and (b) the convective occurrence field for day 314. The white contour lines in (a) and (b) indicate the edge of the moist region (60 mm) and of the convectively active region, respectively. Both fields are shifted such that the center of mass of the moist/convectively active region lies in the center of the domain. The definitions of the convective occurrence field and the convectively active region are given in the text.

the observed SST profile, they found that precipitation peaks about 6° off the peak SST (see their Figure 13). While all the above-described instances of edge intensification refer to idealized simulations, Klocke et al. (2017) noted that "convection is most intensive on either flank of the doldrums" in realistically configured convection-permitting simulations of the tropical Atlantic. In addition to these numerical simulations, there is also an indication for edge intensification in observations. Using satellite observations of CWV, Mapes et al. (2018) show that over tropical oceans there is a sharp boundary between moist and dry regions. Calculating the mean precipitation rate as a function of the meridional distance to this boundary they found a plateau of almost constant CWV with precipitation intensified close to the edge of this region (see their Figure 3).

In this paper, we study the intensification of deep convection at the edge of the self-aggregation cluster in a RCE study, that is, in the absence of any imposed gradient in SST or insolation and without rotation, and investigate the cause of edge intensification therein. A method to determine the strength of deep convection at a given distance from the edge of the moist region is introduced in section 2. In section 3, we first show that deep convection tends to peak at the edge of the moist region but only during times in which the moist region is comparatively large. We then analyze possible reasons for this edge intensification by comparing the spatial distribution of deep convection with the spatial distribution of other variables known to be important for the life cycle of deep convection. In section 4, we discuss the importance of cold pools for edge intensification. A possible explanation of the dependence of edge intensification on area is discussed in section 5. The results of this study are summarized in section 6.

2. Methods

2.1. Simulation

In this study, we analyze the spatial distribution of deep convection in a numerical simulation of RCE, performed with the University of California Los Angeles large-eddy simulation model coupled to a slab ocean. Radiation is calculated interactively. In particular, we use the U50D simulation previously described in Hohenegger and Stevens (2016) where U denotes the model (University of California Los Angeles large-eddy simulation), 50 denotes a slab ocean depth of 50 m, and D denotes the presence of a diurnal cycle in the insolation. The horizontal grid spacing of the domain is 3 km, and the horizontal domain size is 576 km × 576 km. In the vertical, there are 63 levels with a grid spacing that increases from the surface to the top of the atmosphere as $\Delta z = 75\text{m} \cdot 1.05^n$, where n is the level index starting at the surface. The initial sounding was obtained from a simulation on a smaller domain (192 km × 192 km) with a fixed SST of 301 K. Note that no mean wind or wind shear is imposed. While a number of different RCE simulations are discussed in Hohenegger and Stevens (2016), we here use this particular simulation because of the exceptionally long integration period of 600 days. This long integration period allows us to derive robust statistics given the internal variability of the atmospheric fields in the steady state. The setup of the simulation is, apart from the long integration period, comparable to many previous RCE studies, though the presence of a slab ocean is uncommon as SSTs are usually fixed. We expect that the presence of the slab ocean will not significantly

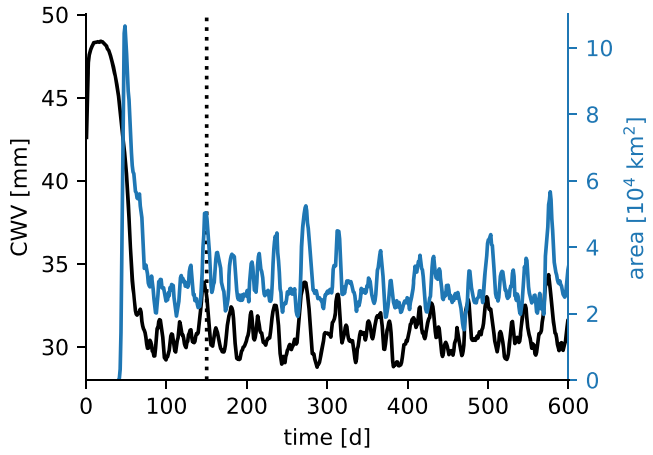

Figure 2. Time evolution of the domain mean CWV (black) and the area of the moist region (CWV≥60mm, blue). The dotted line marks the beginning of the simulation period analyzed in this study.
CWV = column-integrated water vapor.

impact the phenomena and mechanisms discussed in this study as the steady state of the here discussed simulation strongly resembles the steady state of the U500D simulation of Hohenegger and Stevens (2016), that is, a simulation where the slab ocean is 500 m deep and thus the impact of the slab ocean is expected to be small. For a more detailed description of the model, its coupling to a slab ocean and the experimental setup, see Hohenegger and Stevens (2016).

As expected, the simulation shows self-aggregation, where the initially homogeneous humidity field eventually separates into a moist and a dry region, with all deep convection confined to the moist region (see Figure 1). The time evolution of self-aggregation in the simulation analyzed here can be seen in Figure 2. The time evolution is shown in terms of the domain mean CWV, which decreases when the degree of organization increases (e.g., Bretherton et al., 2005). The time evolution of the mean CWV in Figure 2 thus indicates an increase in the degree of organization for about 100 days, before reaching a new steady state. The steady state is, similar to what has been found in previous studies, described by a single, almost circular moist region where all the deep convection is aggregated. In this study, we focus on the properties of this steady state and choose as analysis period day 150 to day 600. As is apparent in Figure 2, the fully aggregated state is not completely steady but shows statistical fluctuations that were also apparent in previous RCE studies, which showed self-aggregation (e.g., Figure 5 in Bretherton et al., 2005) and which have recently been discussed in the context of an oscillation (Patrizio & Randall, 2019).

2.2. Distance Metric

As stated in the introduction, deep convection in RCE studies that show self-aggregation is known to be limited to the moist part of the domain. In section 3, we use the above-described simulation to address the question of how deep convection is distributed within the moist region and what controls this distribution. To do so, we study variations in atmospheric variables as a function of the distance to the edge of the moist region. The moist region is defined as the region where the daily averaged CWV is larger than or equal to 60 mm, though sensitivity studies show that the main results presented here remain the same for meaningful values of the chosen threshold. As an example, the resulting edge is indicated by the white contour line in Figure 1a.

To determine mean statistics, for example, for the convective occurrence field at a given distance from the edge, we first determine the distance from the edge of the moist region for each grid cell by calculating its minimum distance to the edge. To differentiate between the inside and the outside of the moist region, all values outside of the moist region are multiplied by minus one. This defines a distance field $D(x,y)$ that we can use to compute the averaged value $F(x,y)$ of any 2-D field as a function of the distance d from the boundary:

$$F(d) = \frac{1}{|D(x,y) \in [d, d+\Delta d]|} \sum_{D(x,y)\in[d,d+\Delta d]} F(x,y). \quad (1)$$

Note that in the following, we set Δd equal to 7 km and that unless stated otherwise, we use daily averaged fields for both $D(x,y)$ and $F(x,y)$.

Note that the diagnostic derived above can be applied to any other field of interest. In section 4, for example, we apply the diagnostic using the field of convective occurrence, rather than CWV, to calculate $D(x,y)$. Convective occurrence is defined by the number of times per day the cloud water content at 4 km exceeds 0 g/kg. As we use the 2-hourly output for the cloud water content, the maximum number of convective occurrences per day is 12. The reason for using the convective occurrence field instead of CWV is that it more accurately identifies the region of deep convective activity. One difficulty in using the convective occurrence field is, however, that it is too noisy to define a single convective region. We, therefore, apply a 2-D Gaussian smoothing before determining the edge of the convectively active region; see white contour in Figure 1b. Due to the smoothing process we also need to choose a value slightly larger than 0 to define the edge (here defined

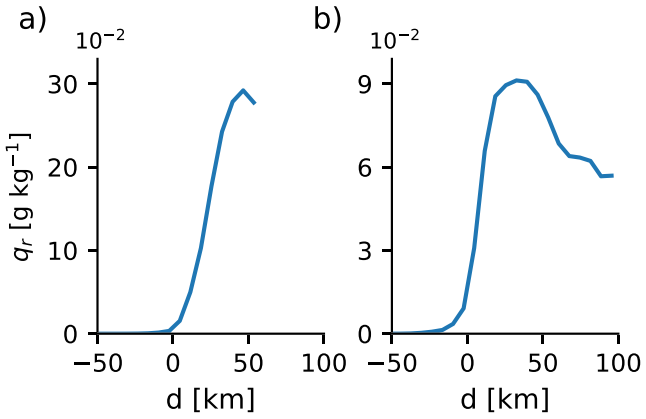

Figure 3. Mean rainwater mixing ratio in the lowest model level as a function of the distance from the edge of the moist patch for the (a) 5% smallest and (b) 5% largest moist patches. Note that the *y* axis has different scales in (a) and (b).

by the location where the smoothed convective occurrence field is equal to 0.01). As shown in Appendix A, our results are not very sensitive to the chosen smoothing strength or threshold.

3. Edge Intensification of Convection

Analyzing how the strength of deep convection, as measured by the rainwater mixing ratio in the lowest model level, changes as a function of the distance from the edge of the moist region, we find that deep convection is edge intensified but only if the size of the moist patch is large (Figure 3). For each day of the here analyzed period (150 to 600 days), there is a unique moist patch whose size significantly fluctuates as apparent from Figure 2. Figure 3 shows that the rainwater mixing ratio is significantly edge intensified for the 5% largest moist areas but not for the 5% smallest moist areas. In particular, the rainwater mixing ratio for the largest areas drops from $9.1 \cdot 10^{-2}$ g/kg at the edge to $5.7 \cdot 10^{-2}$ g/kg in the center of the moist region. In addition to the difference in edge intensification between large and small areas, Figure 3 also reveals larger values of rainwater mixing ratio in case of the smaller area and vice versa. While the dependence of the mean atmospheric state and the dependence of edge intensification on the size of the area will be discussed in section 5, we first aim at explaining the cause for edge intensification and therefore first focus on the times during which the area is larger than the 95th percentile.

3.1. Comparison of Mechanisms

To understand the cause of edge intensification, we compare the spatial distribution of deep convection with the spatial distribution of variables that are generally believed to control the life cycle of deep convection: CWV, convective available potential energy (CAPE), convective inhibition (CIN), latent heat flux (LHF), sensible heat flux (SHF), and surface convergence. As edge intensification can be due to stronger and/or more numerous updrafts at the edge, we try to distinguish between variables that impact the strength of updrafts and variables that impact the probability of triggering new updrafts. To this end, we divide the above-listed variables into two categories.

Updraft strength:

- CWV (in particular free tropospheric humidity): determines how much the buoyancy is reduced by entraining air from the surrounding
- CAPE: determines the buoyancy of an undiluted parcel

Triggering of updrafts:

- CIN: determines the energy input needed to lift a parcel to the level of free convection
- Surface fluxes: determine buoyancy flux and the rate at which heat and moisture are supplied to the boundary layer
- Surface convergence: measures the strength of mechanical lifting

Note that CAPE and CIN are computed columnwise by adiabatically lifting an imaginary parcel from the lowest model level to the model top. In particular, CIN and CAPE are calculated from the difference between the virtual temperature of the air parcel and the virtual temperature profile of the environment, here approximated by the domain mean profile. As we use the same approach as Moseley et al. (2016), calculation details and definitions can be found in the Method section of Moseley et al. (2016).

According to the categorization above, Figures 4a and 4b suggest that edge intensification is not due to stronger updrafts at the edge of the moist region as neither CWV nor CAPE is increased there. In particular, Figure 4a shows that while CWV steadily increases toward the moist region, it levels off to an approximately constant value of 70 mm inside the moist region. We note that CWV values of 70 mm are at the upper end of CWV values observed in the tropics (see, e.g., Peters & Neelin, 2006; Holloway & Neelin, 2009). It is, in fact, interesting to note that while deep convection has been shown to increase rapidly with CWV, this sensitivity becomes less pronounced for these extremely high values of CWV (e.g., Peters & Neelin, 2006). There thus appears to be little room for an additional positive effect of CWV on the updraft strength. CAPE, In contrast

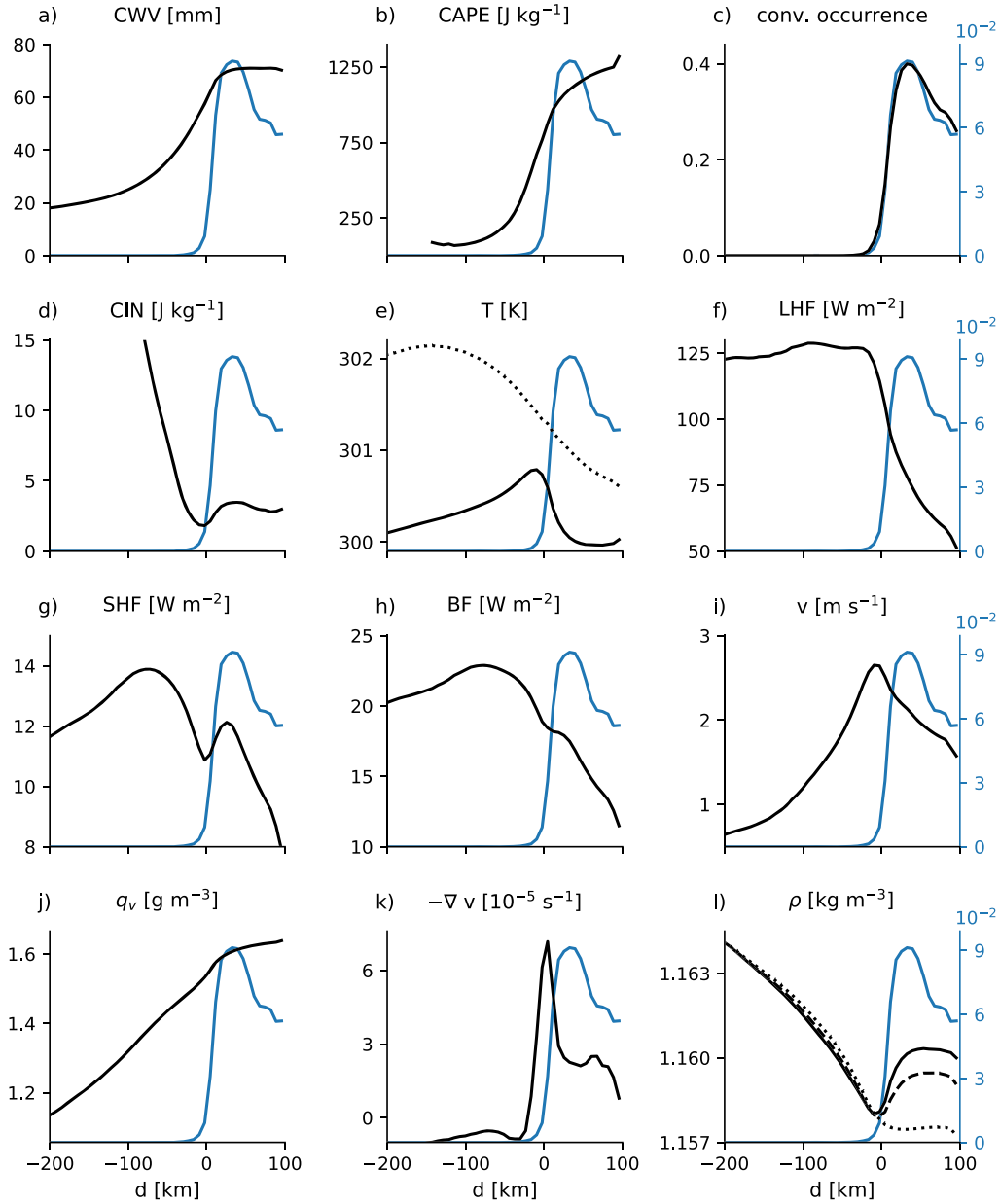

Figure 4. Mean dependence on the distance from the edge of the moist region of (a) column-integrated water vapor, (b) CAPE, (c) convective occurrence, (d) CIN, (e) air temperature in the lowest model level and sea surface temperature (dotted), (f) latent heat flux, (g) sensible heat flux, (h) buoyancy flux, (i) horizontal wind speed in the lowest model layer, (j) water vapor mixing ratio at 100 m, (k) convergence at the surface, (l) density in the lowest layer (solid), 200-m (dashed), and 400-m (dotted) height. To compensate for the general decrease of density with height, the 200- and 400-m density dependencies are shifted such that the density of each layer overlaps with the surface density at $d = -200$km, at which ρ in 200 m is 1.151 kg/m^3 and ρ in 400 m is 1.128kg/m^3. All dependencies are calculated for the largest 5% of the moist patches only, including the dependence of the rainwater mixing ratio in the lowest model level which is included as reference in each plot (blue). CWV = column-integrated water vapor; CAPE = convective available potential energy; CIN = convective inhibition; LHF = latent heat flux; SHF = sensible heat flux; BF = buoyancy flux.

to the CWV, increases not only up to the boundary of the moist region but all the way to the center of the moist region; see Figure 4b.

Considering CAPE, the most buoyant and thus strongest convection might therefore be expected to form in the center of the domain rather than at the edge, in particular because the high values of CWV suggest that entrainment will only weakly reduce the buoyancy. Considering the spatial distribution of CWV and CAPE,

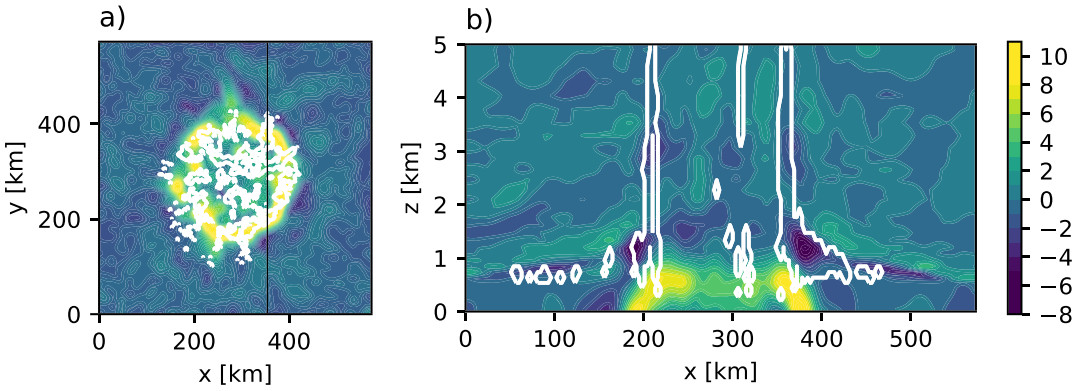

Figure 5. (a) Daily averaged and smoothed surface convergence (color scale, unit: 10^{-5} s^{-1}) and instantaneous liquid water path (white contour: 0.1 mm) for the sample day shown in Figure 1, the black line indicates the location of the cross section shown in (b). (b) Cross section of convergence field (color scale, unit: 10^{-5} s^{-1}) and liquid water mixing ratio (white contour: 0.1 g/kg).

we therefore conclude that the moist region is a region which is very favorable for the formation of deep convection but that variations of these variables within the moist region cannot explain edge intensification. This suggests that edge intensification is due to the preferential triggering of convection at the edge of the moist region. This is first confirmed by the frequency of deep convective occurrence (Figure 4c), whose spatial variation mirrors the spatial variation of precipitation. It is also confirmed by the spatial variations of some of the variables relevant for triggering.

In the simulation investigated here, CIN is generally quite low within the moist region, with values below 5 J/kg, but particularly so at the edge, see Figure 4d. This difference in CIN between the edge and the center of the moist region appears to be due to differences in the air temperature close to the surface, which is higher at the edge than in the center (Figure 4e). The small values of CIN at the edge of the moist region suggests that convection can easily be triggered there. For a given value of CIN, the probability of overcoming this energy barrier can be expected to depend on the buoyancy flux and mechanical lifting. Instead of directly considering the buoyancy flux, we here first analyze the LHF (Figure 4f) and the SHF (Figure 4g), separately, before considering the buoyancy flux, which we approximate as SHF+0.07LHF (Figure 4h).

Figure 4f shows that the LHF is marked by high, approximately constant values in the dry region but quickly decreases when approaching the edge of the moist region and keeps on decreasing in the inside of the moist region. The spatial progression of the LHF does not reflect the progression of the precipitation and thus cannot explain edge intensification. The higher values of the LHF in the dry region result from the much drier boundary layer in this region. Its approximately constant value appears to result from the compensating effect of a simultaneous increase in surface velocity (see Figure 4i) and boundary layer humidity (see Figure 4j).

Compared to the LHF, the dependence of the SHF on d is more complicated and exhibits a local maximum at the location where precipitation gets edge intensified. While we discuss how the different drivers of the SHF contribute to this local maximum in the following, we first note that given the small magnitude of the local maximum in SHF, of below 1 W/m^2, it seems unlikely that this small increase in SHF is responsible for the edge intensification. Analyzing the drivers of the SHF, that is, surface velocity (Figure 4i) and air-sea-temperature difference (compare the air temperature and the SST in Figure 4e), shows that the SHF follows the air-sea temperature difference, which has a local minimum at the location of the velocity maximum and a local maximum close to the peak in rainwater mixing ratio. The cause of the peak in surface velocity and the low air temperature inside the moist region will be discussed in detail in section 4. Note that calculating the buoyancy flux from the SHF and the LHF (Figure 4h), we find that the buoyancy flux, as expected, resembles the SHF though the reduced values of the LHF in the moist compared to the dry region lead to an even less pronounced local maximum.

Next, we determine where new convection is likely to be triggered by dynamical lifting by considering the convergence of the horizontal surface wind. Figure 4k shows the strongest signal for edge intensification so far, with a very strong and sharp peak in convergence at the edge of the moist region. This suggests that there

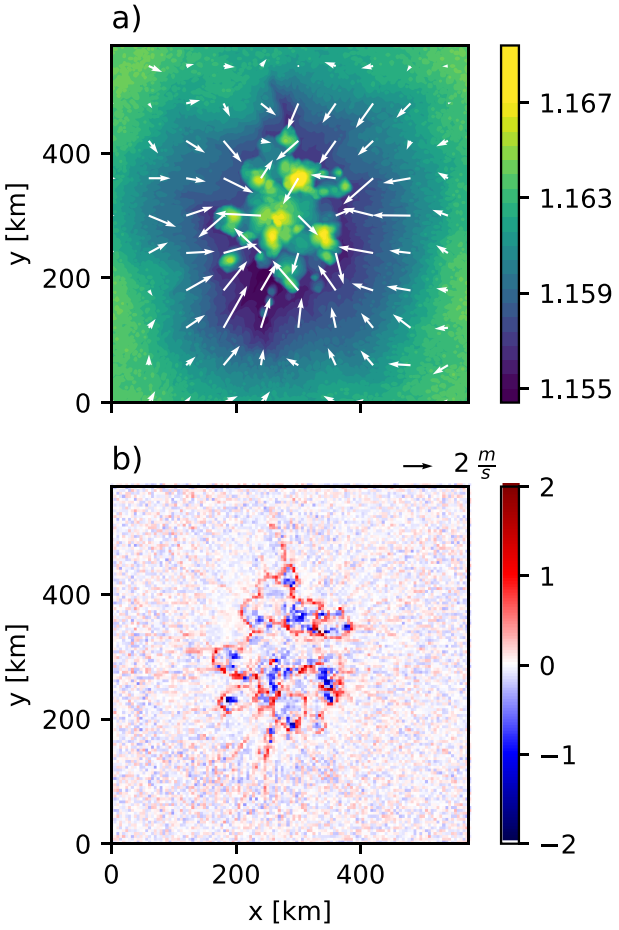

Figure 6. Snapshots of lowest model level (a) density (color scale, kg/m^3) and horizontal wind field (arrows), (b) convergence (color scale, 10^{-3} s^{-1}) for the sample day shown in Figure 1.

is dynamical lifting of air at the edge of the moist region. Together with the decreased values of CIN, this lifting makes the edge of the moist region a favorable place for triggering of deep convection. Although the peak of convergence is very strong and located at the edge of the moist region, it is displaced with respect to the peak in precipitation (compare the black and blue curves in Figure 4k). To understand this shift, we plot in Figure 5 a snapshot of the convergence field and the liquid water content, both in a plane view (Figure 5a) and in a vertical cross section (Figure 5b). Figure 5a shows a closed ring of surface convergence with clouds located almost exclusively on the inside of the surface convergence ring. This results from the convergence being slanted toward the center of the moist region (see Figure 5b) and explains the shift between peak surface convergence and peak precipitation displayed by Figure 4k.

Finally, we note that the strong peak in convergence not only indicates that edge intensification is due to increased triggering at the edge of the moist region and also that edge intensification is due to a dynamical rather than a thermodynamical process. The dominant role of the dynamical processes is particularly apparent when comparing the spatial distribution of deep convection with the low-level convergence on the one hand and with CAPE on the other hand. The comparison of these two variables is interesting considering their respective importance in different parameterization schemes of deep convection. In particular, CAPE and low-level (moisture) convergence have been used as closures for deep convection in convective parameterizations, where the Arakawa-Schubert scheme (Arakawa & Schubert, 1974) and the Tiedtke scheme (Tiedtke, 1989) are respective examples. To further investigate the cause of edge intensification, we will, in the following, focus on explaining the origin of the strong surface convergence at the edge of the moist region.

4. Super-cold-pool

In the following, we will show that the above-discussed peak in surface convergence marks the location where a low-level inflow, directed toward the moist region, hits a positive low-level density anomaly, which spans the precipitating region. Before discussing how the low-level inflow and the surface density anomaly lead to surface convergence we first discuss these two features individually.

The presence of a low-level inflow in the steady state of self-aggregation is expected from previous studies (e.g., Bretherton et al., 2005; Jeevanjee & Romps, 2013; Muller & Held, 2012). In particular, a deep and a shallow circulation combine at the surface to create a low-level inflow directed toward the moist region. Investigating the respective magnitude of the deep and the shallow circulation, Jeevanjee and Romps (2013) find in a RCE simulation with comparable domain length (though a 2-D setup) that both circulations contribute about equally to the low-level inflow. While the deep circulation is directly driven by deep convection, the shallow circulation has been shown to be driven by differential radiative cooling (e.g., Muller & Held, 2012), horizontal anomalies of convective heating (Holloway & Woolnough, 2016) or differences in the low-level water vapor content (Yang, 2018). While we did not investigate the drivers of the shallow circulation in this study, the absence of low-level clouds in the dry region (not shown) suggests that the shallow circulation here is either driven by radiative cooling at the top of the comparatively moist boundary layer or by the virtual effect of water vapor in the boundary layer (see Figure 4j). The resulting strength of the low-level inflow is indicated by the surface wind speed which, as shown in Figure 4i, increases toward the edge of the moist region. That the inflow is indeed directed toward the moist region is suggested by the decrease in density toward the edge of the moist region in Figure 4l. It is also exemplarily shown in Figure 6a.

The rapid decrease in wind speed within the moist region can be explained by the presence of a positive density anomaly in the lowest 400 m (see Figure 4l). These high-density values mainly reflect the colder

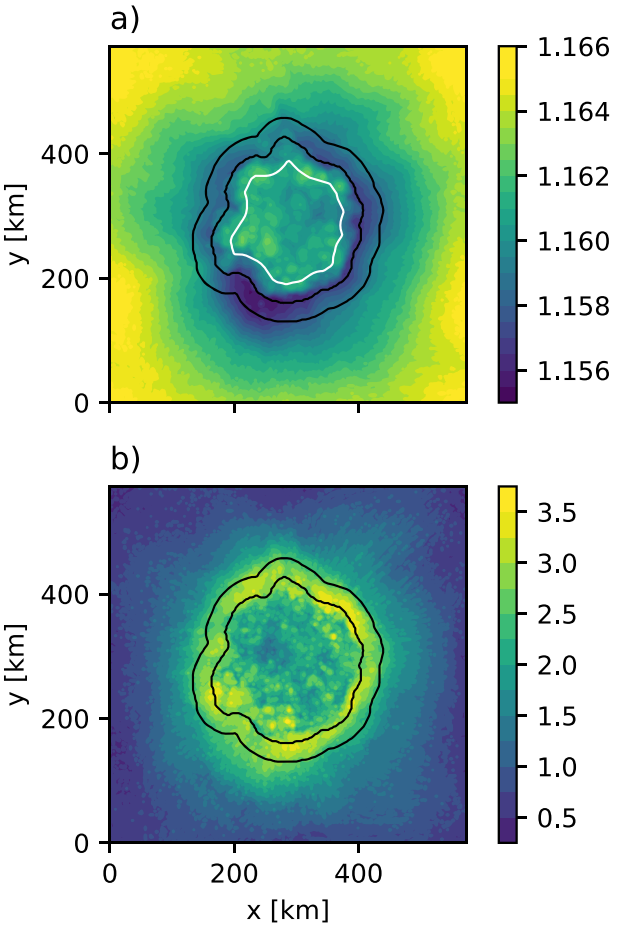

Figure 7. Daily averaged (a) surface density (color scale, kg/m^3) and (b) horizontal surface velocity (color scale, m/s) for the sample day shown in Figure 1. The black lines mark the 6- and −24-km distance from the convectively active region and the white line marks the 36-km line.

air temperatures inside this region (see, e.g., the air temperature in the lowest model layer in Figure 4e). The presence of a confined positive density anomaly, in theory, generates a density current (e.g., Benjamin, 1968), here directed from the cold and moist (dense) toward the warm and dry (less dense) area and opposing the low-level inflow. Figure 6a shows that this density anomaly is composed of multiple smaller-scale density anomalies, which have the signature of convectively driven cold pools (see, e.g., x = 190 km and y = 230 km). The signature of cold pools can also be seen in the surface convergence field (Figure 6b), where the individual cold pools are marked by surface divergence at the center of the cold pool surrounded by a ring of convergence. These convergence lines from the individual cold pools combine to an almost continuous convergence line surrounding the region of high density (see Figure 6b). Visual inspection of the convergence field and the liquid water path field (not shown) suggests, as expected from previous studies (e.g., Schlemmer & Hohenegger, 2014; Tompkins, 2001b), a strong correlation between convection and low-level convergence, in particular we find indications of convection mostly on top of either cold pool centers (i.e., at the location of strong divergence) or cold pool edges (i.e., on top of the surrounding convergence lines). Note that the triggering of deep convection by cold pools has, in fact, been argued to be a possible driver for self-aggregation (Haerter, 2019). Similar to what we find here, their simple model of cold pool interaction suggests that the surface in the convecting region is completely populated by cold pools. In the following, we will argue that the positive low-level density anomaly and the surrounding convergence line results from the combined effect of individual cold pools or, in other words, that the individual cold pools combine to form a "super-cold-pool" with new convection triggered at the edge of the super-cold-pool.

Just like any individual cold pool, the above described super-cold-pool would be expected to expand horizontally in the absence of any opposing forces. As this expansion is however opposed by the low-level inflow these two processes can induce strong convergence at the edge of the moist region but only if the inflow velocity and the expansion rate of the density anomaly approximately balance. To test this, we, therefore, compare the inflow velocity at the edge of the moist region with the expected expansion velocity of the density anomaly. To this end we use the daily averaged surface velocity and density fields, an example of each is shown in Figure 7.

The expected expansion rate of the supercold is estimated using results from Rotunno et al. (1988) for individual cold pools. In particular, they show that the expected cold pool propagation velocity can be estimated as (their equation (16)):

$$v_{\mathrm{cp}} \approx \alpha \left[\int_0^H (-B) \mathrm{d}z \right]^{\frac{1}{2}}, \tag{2}$$

where B is the buoyancy of the air within the cold pool and H is the height of the cold pool. The buoyancy is determined by the density difference between the inside and outside of the cold pool, ρ and ρ_0, respectively, and the acceleration of gravity, g: $B = g(\rho_0 - \rho)\rho^{-1}$. In their calculation, α is equal to $\sqrt{2}$ but they note that experiments suggest a value of α closer to 1. Here, instead of applying equation (2) to individual cold pools, we apply it to the super-cold-pool, that is, the entire low-level density anomaly and refer to the resulting propagation speed as v_{scp}. To calculate the buoyancy of the super-cold-pool in equation (2), we use the daily mean density inside the super-cold-pool ρ^{scp} and in the surrounding of the super-cold-pool ρ_0^{scp}:

$$v_{\mathrm{scp}} \approx \sqrt{2} \left[\int_0^{H_{\mathrm{scp}}} -g \left(\frac{\rho_0^{\mathrm{scp}} - \rho^{\mathrm{scp}}}{\rho^{\mathrm{scp}}} \right) \mathrm{d}z \right]^{\frac{1}{2}}, \tag{3}$$

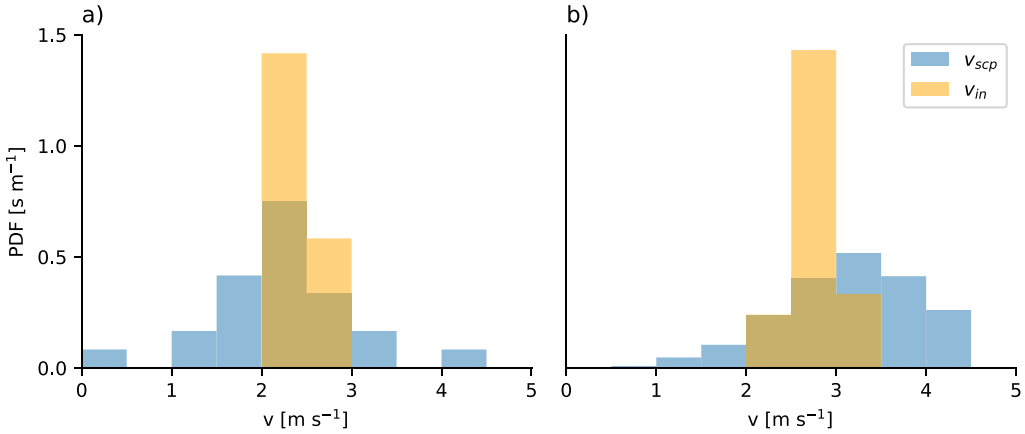

Figure 8. Normalized histogram of the inflow velocity at the edge of the moist region, v_{in}, and the super-cold-pool velocity, v_{scp}, calculated for (a) days 150 to 600 when the area of the moist patch is larger than the 95th percentile (true for 24 days) and (b) days 150 to 600 of the simulation.

where we have set $\alpha = \sqrt{2}$. Based on the edge of the field of convective occurrence, the inside and outside of the super-cold-pool are defined as 36 km $\leq D(x, y)$ and -24 km $\leq D(x, y) \leq 6$ km, respectively. For an example see Figure 7a, where the boundaries of these regions are included as contours. The choice of these specific values is motivated by the dependence of the surface density on the distance from the edge of the convective region shown in Figure 4l, which has its local minimum between about $d = -24$ km and $d = 6$ km and reaches its local maximum inside the moist region at about $d = 36$ km. The height of the super-cold-pool, H_{scp}, is given by the height at which the density inside the super-cold-pool is no longer larger than the density outside. With these definitions we can now calculate v_{scp} for each day, for example, v_{scp} is about 2.3 m/s for the day shown in Figure 7. For each day, the corresponding inflow velocity v_{in} is estimated by averaging the surface velocity field over the region, which we previously defined as the outside of the super-cold-pool, that is, -24 km $\leq D(x, y) \leq 6$ km. As we show in Appendix A, our results are not very sensitive to these choices. Averaging the resulting inflow and super-cold-pool velocities for the days where the area is larger than the 95th percentile, we note that the two velocities have comparable magnitude with a mean inflow velocity of 2.4 m/s and a mean v_{scp} of 2.2m/s. This is further illustrated in Figure 8a, which shows the histogram of the calculated v_{scp} together with the histogram of the inflow velocity, v_{in}. Note that it is not surprising that the above analysis does not yield a better agreement between v_{in} and v_{out} as there are uncertainties connected with the choices we made to calculate the buoyancy as well as in the choice of α. Instead of fine-tuning either the chosen boundaries or α, we note that the key point of this analysis is that the expansion rate of the low-level density anomaly approximately balances the inflow. This balance, as noted at the beginning of this section, can explain the presence of strong low-level convergence and thus the increased triggering of convection at the edge of the moist region.

After explaining the cause for the strong surface convergence it is worthwhile to again consider the shift between the precipitation maximum and the maximum in surface convergence, discussed in section 3. Note that this shift is in contrast to previous cold pool studies where new clouds tend to be located directly on top of peaks in surface convergence/low-level vertical velocities (see, e.g., Figure 4c in Schlemmer & Hohenegger, 2014). As we have seen in Figure 5b, however, the convergence here is slanted, which might be readily explained from the low-level inflow and the slanted low-level density anomaly (see Figure 4l). In contrast, convergence in previous studies might be expected to be more vertically oriented as it often results from the collision of two or more cold pools.

As argued above, cold pools thus play an important role for edge intensification in this study. One difficulty, however, is that the employed resolution of 3 km, while a typical resolution for RCE simulations, is much coarser than the horizontal resolution of studies which explicitly study the properties of cold pools. Grant and van den Heever (2016), for example, note that a horizontal resolution of at least 100 m is necessary to correctly represent the dissipation process of cold pools. While we would therefore expect some of the properties of the here simulated cold pools, and thus also of the resulting super-cold-pool, to change with increasing resolution, the two key ingredients of the presented mechanism are expected to still be present

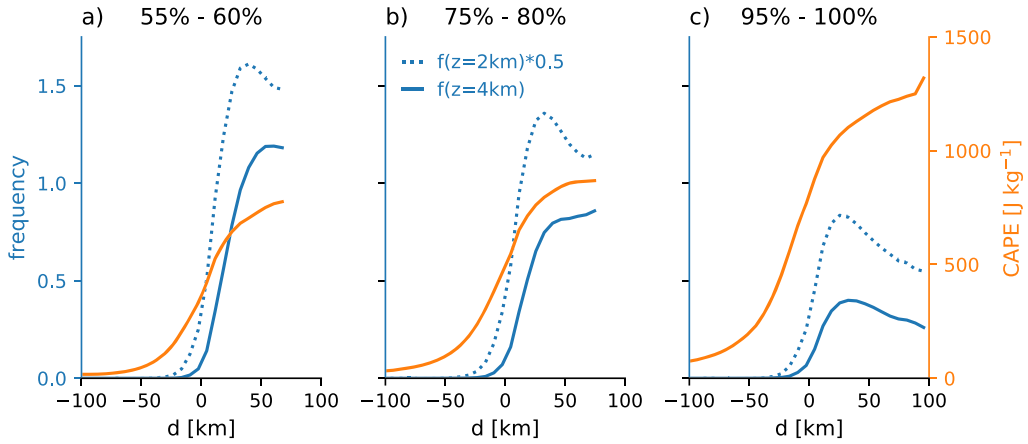

Figure 9. Mean frequency of convective occurrence measured at a height of 4 km (blue solid) and 2 km (blue dotted) are compared to CAPE (orange) for different area ranges. For each area range, all days are used for which the size of the moist area is between (a) the 55th to 60th percentile, (b) the 75th to 80th percentile, and (c) the 95th to 100th percentile. Note that the convective occurrence measured at 2 km is rescaled by a factor 0.5 for better comparison.

in simulations with higher resolution. In particular, using a RCE simulation with higher horizontal resolution (started, e.g., from already aggregated conditions to ensure self-aggregation; Muller & Held, 2012), we would, in the steady state of self-aggregation, expect a low-level inflow directed toward the convective region in which deep convection would still be expected to induce positive low-level density anomalies via cold pools. Changing the resolution is therefore not expected to alter the basic mechanism presented here but might very well impact the properties of the super-cold-pool, which might effect, for example, the size of the convectively active region.

While the above discussion was limited to days during which the moist area is large, it is worth noting that the approximate balance between the inflow velocity and the super-cold-pool propagation velocity also holds if all days in the period from day 150 to day 600 are considered. The corresponding histogram for the entire analysis period can be seen in Figure 8b. The mean inflow velocity is 2.8m/s, while the mean super-cold-pool velocity is 3.2 m/s. Note that the much larger number of days considered in Figure 8b, 450 rather than 24 days, leads to a smoother histogram and hides the single outlier with v_{scp} smaller than 0.5 m/s apparent in Figure 8a. As Figure 8b suggests that there is a balance between the inflow velocity and the super-cold-pool propagation speed and thus also convergence at the edge of the moist region independent of domain size, we will in the following discuss why edge intensification shows a dependency on domain size.

5. Discussion

As noted in section 3, the presence of edge intensification depends on the size of the moist patch. In particular, the intensification of the rainwater mixing ratio at the edge of the moist region is stronger for larger moist areas. This area dependence shown in the rainwater mixing ratio is mirrored by the convective occurrence field (see Figure 9), which shows that the number of convective updrafts which reach a height of at least 4 km only increases at the edge of the largest areas. It is, however, interesting to note that for smaller convective areas edge intensification is still evident for the more shallow convection reaching 2 km only (see Figure 9). This suggests that while the edge is at all times a favorable place for the triggering of convection, the triggered convection does not always grow into deep convection. This result compares well with the finding that the edge is marked by strong convergence and thus an increased likelihood for triggering at all times.

Before discussing a possible explanation of this area dependence, we note that Figure 9 shows that for all area sizes less than half of the convective updrafts detected at 2 km reach a height of 4 km. This difference between the two heights is more pronounced at the edge than at the center of the moist region. Comparing these results with the spatial distribution of CAPE shows that the atmosphere inside the moist region is more unstable to convection than the edge of the moist region, independent of the considered area range. This might explain why more of the updrafts triggered at the center grow to a height of at least 4km. Moreover, updrafts are surrounded only by moist air inside of the moist patch, whereas they are exposed to drier

conditions at the edge. Considering now the area dependence of the two convective occurrence fields, we first note that the reduction of convective updrafts at the edge is less pronounced for the largest moist patches (Figure 9c). In addition, we also note that the magnitude of CAPE for the different area ranges shows significantly larger values of CAPE for the larger areas (e.g., Figures 9a and 9c). These larger values of CAPE might increase the probability for convection, once it has been triggered at the edge of the larger moist regions, to develop into deep convection. Note that the increased values of CAPE for larger areas are due to lower temperature values in the free troposphere (not shown). Interestingly, systematic changes in the large-scale instability during the steady state of self-aggregation have also been discussed by Patrizio and Randall (2019).

6. Conclusion

This paper discusses a phenomenon that we refer to as *edge intensification* of convection and which describes the intensification of precipitation at the edge of a convectively active region. This phenomenon has been found both in idealized and realistic simulations in past studies but has not yet been explained. In this study, we explain edge intensification using an idealized simulation of RCE. We find that precipitation in the RCE simulation is edge intensified but only during times at which the moist, convectively active area is comparatively large. This edge intensification is shown to result from the enhanced triggering of convection at the edge, rather than from increased updraft strength. The enhanced triggering is shown to result from the convergence of a low-level inflow, directed from the dry to the moist region, and a low-level density anomaly, which spans the entire precipitating region. The presence of a low-level inflow is expected from previous RCE studies (e.g., Bretherton et al., 2005; Jeevanjee & Romps, 2013; Muller & Held, 2012), while the density anomaly in the precipitating region is, as we show here, due to the convective cool pools resulting from the deep convection in the moist region. The individual cold pools combine to form a *super-cold-pool*, that is, a persistent low-level density anomaly spanning the entire moist region. Estimating the maximum propagation speed with which the super-cold-pool boundary would expand in the absence of any inflow we show that this velocity approximately equals the inflow velocity. Together, the low-level inflow and the low-level density anomaly create strong convergence at the boundary of the super-cold-pool, that is, at the boundary of the moist region. As for single cold pools, new convection is triggered at the boundary which can thus explain edge intensification for large areas. For small areas, we find that despite the presence of a super-cold-pool and strong convergence at the edge, there is no edge intensification of deep but only of shallow convection. This increased frequency of shallow clouds at the edge shows that there is still increased triggering of convection at the edge but less of the triggered convection evolves into deep convection. Further analysis suggests that for smaller moist areas there is a reduced large-scale instability of the atmosphere compared to larger areas. All in all our results suggest that dynamical effects strongly modulate the spatial distribution of precipitation. In contrast, thermodynamical variables, such as column relative humidity or CAPE, cannot explain edge intensification.

The RCE setup might represent the best case for studying the edge intensification of convection but, given the idealizations, it raises the question as to the importance of the described mechanisms in reality. The Intertropical Convergence Zone (ITCZ) over tropical oceans seems the place of excellence to observe such mechanisms. There is low-level inflow from the subtropics into the tropics resulting from a combination of a deep overturning circulation and a shallow overturning circulation. And there is the presence of several convective systems with their individual cold pools that can combine into a big envelope of convection. As the main difference to our idealized study, though, we might expect to not reach a balance between inflow and outflow but might see cold pools propagating into the drier and thus less favorable regions. This propagation into drier regions, might be facilitated by the fact that cold pools are actually not strongest in the moistest but in intermediate moist regions (Chandra et al., 2018). As a test of our findings, it would be interesting to test whether variability in some measure of the width of the ITCZ correlates with variability in the strength of the cold pools and the low-level inflow. From our results, we would expect a wider ITCZ under situations favoring stronger cold pools and/or weaker inflow.

Appendix A: Sensitivity Tests for the Calculation of the Super-cold-pool Speed

A number of nonunique choices have been made for the calculation of the super-cold-pool speed v_{scp} in section 4. To identify the region of deep convective activity, we start by smoothing the field of convective occurrence and then the convective region corresponds to the region where this smoothed field is larger than a chosen threshold value (tr_c). Smoothing is necessary as we need to find a single, connected region

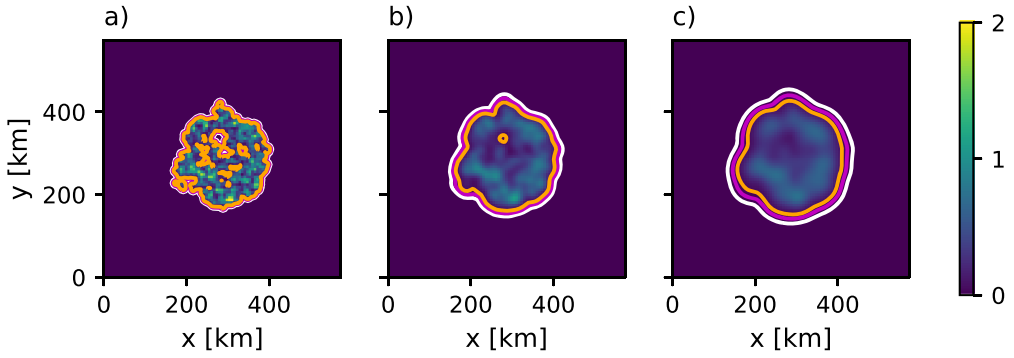

Figure A1. Convective occurrence field shown in Figure 1b after smoothing with different choices of σ: (a) $\sigma = 1$, (b) $\sigma = 3$, and (c) $\sigma = 5$. The contour lines indicate different values of tr_c, where white, magenta, and orange represent 0.001, 0.01, and 0.05 respectively.

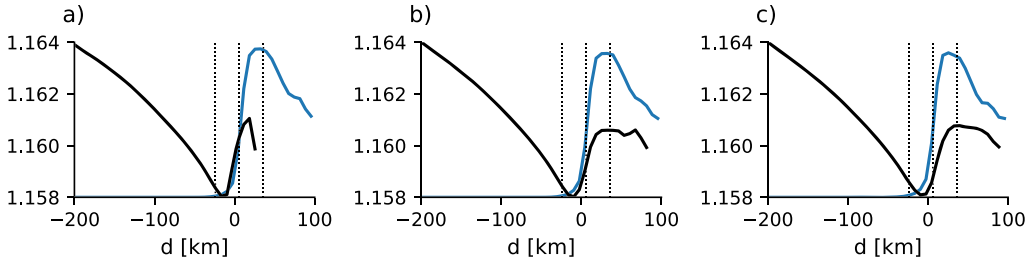

Figure A2. As the solid lines in Figure 4l but for different values of σ: (a) $\sigma = 1$, (b) $\sigma = 3$, and (c) $\sigma = 5$. The vertical lines denote the limits used for calculating v_{scp}.

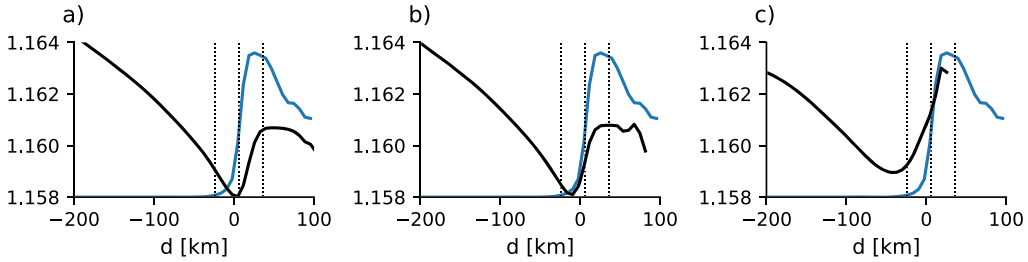

Figure A3. Same as Figure A2 but for different values of the threshold: (a) 0.001, (b) 0.01, and (c) 0.05. The vertical lines denote the limits used for calculating v_{scp}.

of convective activity from the field of convective occurrence which is very noisy (see Figure 1b). For the filtering, we use a Gaussian kernel and thus the strength of the smoothing is given by σ, which denotes the standard deviation of the kernel. The value used in the paper is $\sigma = 3$. The effect of changing σ can be seen in Figure A1 together with three different values of tr_c. The value of tr_c in the main part of the paper is 0.01. As immediately apparent from Figure A1, there is no unique choice of σ and tr_c to define a single region of deep convective activity, though too week smoothing or a too high value of the threshold leads to the identification of multiple convective regions while too strong smoothing or a too low value of the threshold does not capture the region of deep convective activity very well.

To test how the results presented in the main section depend on these choices, we first show how the density distribution of the largest moist areas depends on σ (Figure A2) and on the chosen tr_c (Figure A3). We find that the density distribution, which is the essential distribution for calculating the supercold velocity is comparatively insensitive to the choices of σ and tr_c as long as their combination allows the detection of one single cluster. In all cases, precipitation is intensified at the edge and the density shows a minimum at the edge and a secondary maximum in the moist region (as in Figure 4l), confirming our previous results.

Table A1
Inflow and Super-cold-pool Velocities for Differently Defined Regions (Averaged Over Days 150 to 600 and Only the Days Where the Moist Area Is Larger Than the 95th Percentile)

out. min./out. max./in. (km)	$v_{in}^{\text{all days}}$ (m/s)	$v_{scp}^{\text{all days}}$ (m/s)	$v_{in}^{95\text{th}}$ (m/s)	$v_{scp}^{95\text{th}}$ (m/s)
−24/6/36	2.8	3.2	2.4	2.2
−40/0/40	2.6	3.0	2.4	2.1
−20/20/60	2.7	3.3	2.4	2.3
−10/10/60	2.8	3.4	2.4	2.3
−10/10/20	2.8	3.0	2.4	1.9

An other set of choices that has to be made to calculate the super-cold-pool velocity are the distances from the edge of the convectively active region that were chosen to be $-24\text{ km} \leq D(x,y) \leq 6\text{ km}$ for the outside region and $36\text{ km} \leq D(x,y)$ for the inside region. Table A1 shows the corresponding velocities using different definitions of the regions. It suggests that neither the super-cold-pool velocities nor the inflow velocities are very sensitive to these choices. Hence, the computed super-cold-pool velocity remains robust as long as a unique convective area is identified and the location of the positive density anomaly is well captured.

Acknowledgments
This work was funded by the German Federal Ministry of Education and Research (BMBF) within the framework program "Research for Sustainable Development (FONA)," www.fona.de, under 01LK1507A through the High Definition Clouds and Precipitation for Climate Prediction (HD(CP)2) project. Primary data and scripts used in the analysis and other supporting information that may be useful in reproducing the author's work are archived by the Max Planck Institute for Meteorology and can be obtained via http://hdl.handle.net/21.11116/0000-0004-5169-B website.

References

Arakawa, A., & Schubert, W. H. (1974). Interaction of a cumulus cloud ensemble with the large-scale environment, Part I. *Journal of the atmospheric sciences*, *31*, 674–701. https://doi.org/10.1175/1520-0469(1974)031<0674:IOACCE>2.0.CO;2

Becker, T., Bretherton, C. S., Hohenegger, C., & Stevens, B. (2018). Estimating bulk entrainment with unaggregated and aggregated convection. *Geophysical Research Letters*, *45*, 455–462. https://doi.org/10.1002/2017GL076640

Benjamin, T. B. (1968). Gravity currents and related phenomena. *Journal of Fluid Mechanics*, *31*, 209–248. https://doi.org/10.1017/S0022112068000133

Bretherton, C. S., Blossey, P. N., & Khairoutdinov, M. (2005). An energy-balance analysis of deep convective self-aggregation above uniform SST. *Journal of the Atmospheric Sciences*, *62*, 4273–4292. https://doi.org/10.1175/JAS3614.1

Bretherton, C. S., Peters, M. E., & Back, L. E. (2004). Relationships between water vapor path and precipitation over the tropical oceans. *Journal of Climate*, *17*, 1517–1528. https://doi.org/10.1175/1520-0442(2004)017h1517:RBWVPAi2.0.CO;2

Chandra, A. S., Zuidema, P., Krueger, S., Kochanski, A., de Szoeke, S. P., & Zhang, J. (2018). Moisture distributions in tropical cold pools from equatorial Indian Ocean observations and cloud-resolving simulations. *Journal of Geophysical Research: Atmospheres*, *123*, 11,445–11,465. https://doi.org/10.1029/2018JD028634

Grant, L. D., & van den Heever, S. C. (2016). Cold pool dissipation. *Journal of Geophysical Research: Atmospheres*, *121*, 1138–1155. https://doi.org/10.1002/2015JD023813

Haerter, J. O. (2019). Convective self-aggregation as a cold pool-driven critical phenomenon. *Geophysical Research Letters*, *46*, 4017–4028. https://doi.org/10.1029/2018GL081817

Hohenegger, C., & Stevens, B. (2016). Coupled radiative convective equilibrium simulations with explicit and parameterized convection. *Journal of Advances in Modeling Earth Systems*, *8*, 1468–1482. https://doi.org/10.1002/2016MS000666

Holloway, C. E., & Neelin, J. D. (2009). Moisture vertical structure, column water vapor, and tropical deep convection. *Journal of the Atmospheric Sciences*, *66*, 1665–1683. https://doi.org/10.1175/2008JAS2806.1

Holloway, C. E., & Woolnough, S. J. (2016). The sensitivity of convective aggregation to diabatic processes in idealized radiative-convective equilibrium simulations. *Journal of Advances in Modeling Earth Systems*, *8*, 166–195. https://doi.org/10.1002/2015MS000511

Jeevanjee, N., & Romps, D. M. (2013). Convective self-aggregation, cold pools, and domain size. *Geophysical Research Letters*, *40*, 994–998. https://doi.org/10.1002/grl.50204

Klocke, D., Brueck, M., Hohenegger, C., & Stevens, B. (2017). Rediscovery of the doldrums in storm-resolving simulations over the tropical Atlantic. *Nature Geoscience*, *10*(12), 891–896. https://doi.org/10.1038/s41561-017-0005-4

Liu, C., & Moncrieff M. W. (2008). Explicitly simulated tropical convection over idealized warm pools. *Journal of Geophysical Research*, *113*, D21121. https://doi.org/10.1029/2008JD010206

Mapes, B. E., Chung, E. S., Hannah, W. M., Masunaga, H., Wimmers, A. J., & Velden, C. S. (2018). The meandering margin of the meteorological moist tropics. *Geophysical Research Letters*, *45*, 1177–1184. https://doi.org/10.1002/2017GL076440

Moseley, C., Hohenegger, C., Berg, P., & Haerter, J. O. (2016). Intensification of convective extremes driven by cloud-cloud interaction. *Nature Geoscience*, *9*, 748–752. https://doi.org/10.1038/ngeo2789

Müller, S. (2019). Convectively generated gravity waves and convective aggregation in numerical models of tropical dynamics. (Doctoral dissertation, Universität Hamburg). https://doi.org/10.17617/2.3025587

Muller, C. J., & Held, I. M. (2012). Detailed investigation of the self-aggregation of convection in cloud-resolving simulations. *Journal of the Atmospheric Sciences*, *69*, 2551–2565. https://doi.org/10.1175/JAS-D-11-0257.1

Nolan, D. S., Tulich, S. N., & Blanco, J. E. (2016). ITCZ structure as determined by parameterized versus explicit convection in aquachannel and aquapatch simulations. *Journal of Advances in Modeling Earth Systems*, *8*, 425–452. https://doi.org/10.1002/2015MS000560

Patrizio, C. R., & Randall, D. A. (2019). Sensitivity of convective self-aggregation to domain size. *Journal of Advances in Modeling Earth Systems*, *11*, 1995–2019. https://doi.org/10.1029/2019MS001672

Peters, O., & Neelin, J. D. (2006). Critical phenomena in atmospheric precipitation. *Nature Physics*, *2*, 393–396. https://doi.org/10.1038/nphys314

Rotunno, R., Klemp, J. B., & Weisman, M. L. (1988). A theory for strong, long-lived squall lines. *Journal of the Atmospheric Sciences*, *45*(3), 463–485. https://doi.org/10.1175/1520-0469(1988)045h0463:ATFSLLi2.0.CO;2

Schlemmer, L., & Hohenegger, C. (2014). The formation of wider and deeper clouds as a result of cold-pool dynamics. *Journal of the Atmospheric Sciences*, *71*, 2842–2858. https://doi.org/10.1175/JAS-D-13-0170.1

Tiedtke, M. (1989). A comprehensive mass flux scheme for cumulus parameterization in large-scale models. *Monthly Weather Review*, *117*, 1779–1800. https://doi.org/10.1175/1520-0493(1989)117<1779:ACMFSF>2.0.CO;2

Tompkins, A. (2001a). On the relationship between tropical convection and sea surface temperature. *Journal of Climate*, *14*, 633–637. https://doi.org/10.1175/1520-0442(2001)014h0633:OTRBTCi2.0.CO;2

Tompkins, A. M. (2001b). Organization of tropical convection in low vertical wind shears: The role of cold pools. *Journal of the Atmospheric Sciences*, *58*, 1650–1672. https://doi.org/10.1175/1520-0469(2001)058<1650:OOTCIL>2.0.CO;2

Wing, A. A., & Cronin, T. W. (2016). Self-aggregation of convection in long channel geometry. *Quarterly Journal of the Royal Meteorological Society*, *142*, 1–15. https://doi.org/10.1002/qj.2628

Wing, A. A., Reed, K. A., Satoh, M., Stevens, B., Bony, S., & Ohno, T. (2018). Radiative-convective equilibrium model intercomparison project. *Geoscientific Model Development*, *11*, 793–813. https://doi.org/10.5194/gmd-11-793-2018

Yang, D. (2018). Boundary layer diabatic processes, the virtual effect, and convective self-aggregation. *Journal of Advances in Modeling Earth Systems*, *10*, 2163–2176.